Astronomy & Astrophysics

Inclination effects in T Tauri star spectra

Immo Appenzeller[1] and Claude Bertout[2]

[1] Landessternwarte, Königstuhl 12, 69117 Heidelberg, Germany
e-mail: iappenze@lsw.uni-heidelberg.de
[2] Institut d'Astrophysique, 98bis Bd. Arago, 75014 Paris, France
e-mail: claude.bertout@obspm.fr

ABSTRACT

Context. Because of the presence of rotation and accretion disks, classical T Tauri stars have symmetry planes that are normally inclined relative to the plane of the sky. The inclination angles affect the observed spectral properties of these objects.
Aims. We study the influence of the inclination angles on classical T Tauri star spectra in an empirical manner.
Methods. Published inclination angles, derived from the stellar photospheric rotation or from spatially resolved circumstellar disk observations, are compared with various observed spectral properties, and correlations are established and investigated.
Results. Inclinations derived from the stellar rotation are found to be much less accurate than the published disk inclinations, and no significant correlations between spectral properties and inclinations based on rotation data could be detected. In contrast, significant correlations are found between the disk inclination angles and the apparent velocities observed for the forbidden emission lines and the wind absorption features of permitted lines. These data support the assumption of cone-like polar winds with opening angles smaller than ≈45°. Other spectral features show weaker or no inclination dependence. Using these results, the true (deprojected) flow velocities of the polar winds are derived for the investigated sample of T Tauri stars. Deprojected wind-ejection velocities appear to differ by a factor of two among the stars in our sample, which spans a range of mass-loss rates from 10^{-10} $M_\odot$/yr to 3×10^{-7} $M_\odot$/yr.

Key words. stars: formation – stars: pre-main sequence – stars: rotation – stars: winds, outflows

1. Introduction

Classical T Tauri stars (CTTSs) are low-mass pre-main sequence objects with active accretion disks (e.g., Bertout et al. 1988). The accretion flow to the stellar surface of CTTSs is known to take place along magnetic flux tubes that are anchored to the central stars (e.g., Camenzind 1990). The theory of the formation of low-mass stars predicts that the rotational equatorial planes of the stars and the planes of the accretion disks are similar (see, e.g., Yorke et al. 1993), although the symmetry planes of the magnetic fields may differ (e.g., Bouvier et al. 2007; O'Sullivan et al. 2005). Theoretical models of the star-disk systems and their line-emitting regions reproduce the basic observed properties of the CTTSs fairly well (see, e.g., Hartmann et al. 1994; Kurosawa et al. 2011).

However, the details of the observed spectra are expected to depend on the inclination angles of the individual stars. In addition to the inclination-dependent rotational broadening of the photospheric absorption lines, major effects on the emission line profiles and the strength and width of selected lines have been theoretically predicted (e.g., Muzerolle et al. 2001; Kurosawa et al. 2006). But comparisons of the theoretically predicted inclination dependence with observed spectra have so far led to inconclusive results (e.g., Edwards et al. 1994; Kwan et al. 2007). Therefore, in the present study we identify inclination-dependent spectral features in CTTS spectra in a purely empirical way by comparing observed spectral properties with inclinations inferred from observations. As input data we use published empirically derived inclinations, which are based either on the rotational properties of the corresponding stars or on spatially resolved observations of their circumstellar disks.

2. The database

This study is based on a sample of 45 CTTSs with well studied spectra, for which direct or indirect inclination information is available in the literature. A list of these stars and some relevant spectral data are given in Table 1. In 23 cases, accurate inclinations derived from spatially resolved circumstellar disks are given. For 21 stars we include inclination values derived by comparing projected rotational velocity values $v \sin i$ with the rotational periods observed for the same stars. Since we found a tight correlation between disk inclinations and the velocities of strong forbidden lines, we supplemented our sample of stars with published inclination data by 11 CTTSs with prominent forbidden line emission. In Table 1 these stars are listed without inclination values. Of course, these stars could not contribute to establishing inclination-dependent correlations, but they allowed us to increase the statistical significance of the correlations between the different inclination-sensitive spectral features discussed in Sect. 4.

Two of the stars without direct inclination information (GG Tau and UY Aur) are members of close multiple systems where the inclinations of circumbinary disks or rings are known. These inclinations are not listed in Table 1 because there are close young binaries with misaligned disks (Roccatagliata et al. 2011). Thus, inclinations of the circumbinary disks may not be representative of the circumstellar disk inclinations, which in both cases are known to be present in these systems. Also omitted in Table 1 are the published disk inclination values of the stars DN Tau, DO Tau, and DQ Tau. Although inclination values for the circumstellar disks of these objects are quoted in the *Catalog of Resolved Disks*, which is maintained

Table 1. CTTSs used for this study, listed following the order of the Herbig-Bell catalog of Orion population stars (HBC).

HBC	Object	i_{rot} deg	Ref.	i_{disk} deg	Ref.	Vbe[O I] km s^{-1}	Vb[N II] km s^{-1}	Ref.	$FWHM$(Hα) km s^{-1}	$FWQM$(He I) km s^{-1}	BAc(Hα) km s^{-1}	BAe(He I) km s^{-1}
25	CW Tau					−147	−109	12	465	290	−110	w
26	FP Tau					−86		10	233	122	−47	−84
28	CY Tau	72	1	31	18	−138		10	189	91	w	−161
30	DD Tau					−79	−80	10	195	69	−50	−58
32	BP Tau	32	2	36	18	−31		10	315	70	w	w
33	DE Tau	57	2			−148		10	300	125	−55	w
34	RY Tau			66	19	−115		12	450	w	−40	
35	T Tau N	15	1	20	6	−180		15	275	225	−190	
36	DF Tau	50	2			−103	−84	12	295	75	−63	−163
37	DG Tau	58	2	32	18	−276	−219	10	225	285	−200	−383
38	DH Tau	58	1			−50		12	167		w	
43	UX Tau A	60	1	46	23				125	w	−155	−95
45	DK Tau	44	2			−138		10	320	65	−45	−209
48	HK Tau B			85	16	−22	−17	13	37	51	w	
	HH 30*			82	18	−19	−12	13	50	57	w	
49	HL Tau			40	24	−198	−171	13	239	275	−148	−300
50	XZ Tau					−133	−75	12	110		w	−177
52	UZ Tau E			56	25	−155	−91	12	194	109	−44	−110
54	GG Tau	56	2			−138		10	240	190	−100	w
56	GI Tau	54	1			−69		10	165	68	−45	w
57	GK Tau	46	2			−35		10	300	45	−30	−77
58	DL Tau	78	2	40	18	−203	−188	10	260	281	−150	−191
60	HN Tau					−133	−81	12	289	150	w	w
61	CI Tau			46	25	−179		10	228	202	−113	−167
63	AA Tau	69	2	75	26	−55	−41	10	210	75	−20	−70
65	DN Tau	30	2			−48		10	195	45	−58	w
67	DO Tau					−121		10	200	58	−100	−158
418	HV Tau C			84	17	−41	−25	13	98	109	w	
72	DQ Tau					−52		10	240	115	w	w
74	DR Tau	15	4	20	7	−186	−166	10	175	145	−225	−330
75	DS Tau					−72		10	300	50	−40	−140
76	UY Aur					−103		10	200	68	w	−135
77	GM Aur	90	1	52	18	−19		10	315	140	−75	
80	RW Aur A	37	2			−221		10	490	125	−75	
85	GW Ori	30	5	10	7				180		w	−379
250	GQ Lup	27	3			−38		22	297	67	−13	
251	RU Lup			28	7	−171	−173	11	258	220	w	
	KH15D			84	14	−35		14	121		−7	
568	TW Hya	18	9	8	8	−12		20	190	129	−45	−260
578	VZ Cha					−16		21	166	74	w	
590	HM 32					−14		11	173	58	w	
254	AS 205 A			47	25	−237		11	183	269	−180	
286	S CrA N			<45	7	−139		11	426	120	−85	
291	VV CrA					−257	−175	11	218	226	−310	
292	AS 353 A			20	27	−352		10	275	335	−250	−279

Notes. The first column gives the HBC object number. The following columns give the most common object name, the inclination derived from the stellar rotation (i_{rot}) and the corresponding reference, the inclination derived from the disk aspect angle (i_{disk}) and the corresponding reference, the radial velocity of the blue edge (measured at 25% intensity) of the 630 nm [O I] line, the velocity of the blue peak of the [N II] 658.3 nm line, the reference to the forbidden-line data, the Hα FWHM line width, the FWQM width of the 587.6 nm He I line, the central velocity of the blueshifted wind absorption feature in the Hα emission line (BAc(Hα)), and the blue edge (measured at 25% depth) of the blueshifted wind absorption feature of the 1083 nm He I line (BAe(HeI)). w indicates that the corresponding feature could not be detected or measured.

References. (1) Bouvier et al. (1995); (2) Bouvier (2004, priv. comm.); (3) Broeg et al. (2007); (4) Alencar et al. (2001); (5) Shevchenko et al. (1998); (6) Ratzka et al. (2009); (7) Schegerer et al. (2009); (8) Akeson et al. (2011); (9) Alencar & Batalha (2002); (10) Hartigan et al. (1995); (11) Hamann (1994); (12) Hirth et al. (1997); (13) Appenzeller et al. (2005); (14) Hamilton et al. (2003); (15) Böhm & Solf (1994); (16) Stapelfeldt et al. (1998); (17) Stapelfeldt et al. (2003); (18) Guilloteau et al. (2011); (19) Isella et al. (2010); (20) Herczeg et al. (2007); (21) Krautter et al. (1990); (22) Appenzeller & Wagner (1989); (23) Tanii et al. (2012); (24) Kwon et al. (2011); (25) Andrews & Williams (2007); (26) Cox et al. (2013); (27) Curiel et al. (1997).

by Karl Stapelfeldt[1], the disks of these three stars are only marginally resolved. Their inclinations are therefore correspondingly uncertain. In one case (AS 353A), the disk inclination has been derived indirectly from the well determined inclination of the associated jet, assuming that the jet propagates in a direction that is normal to the disk plane (as observed in all CTTSs for which this information exists).

For all inclination values listed in Table 1 the sources are given in the corresponding reference columns. Generally the source giving the lowest observational error is quoted. Usually this is also the most recent derivation. In many cases, earlier derivations are mentioned in the references listed in Table 1. Additional references on earlier inclination measurements can be found in the extensive literature lists of the *Catalog of Resolved Disks* cited above.

The references cited in Table 1 give mean errors of the listed disk inclinations between 1 degree and 6 degrees, with an average value of 2.2 degrees. Uncertainties of the disk inclination derivations of this order are confirmed by comparing independent derivations by different authors and by measurements obtained at different wavelengths.

The accuracy of the inclinations derived from the stellar rotation is much lower. As described and discussed first by Weaver (1987) the rotational inclinations are derived by comparing projected rotational velocities $v \sin i$, derived from photospheric absorption-line profiles, with the equatorial rotational velocities v_E. For v_E we have

$$v_E = 2\pi R\, P^{-1}, \tag{1}$$

where R is the stellar radius, and P the observed rotation period. The inclination then follows from the relation

$$i = \arcsin\left[\text{const.} \times (v \sin i)\, P\, R^{-1}\right] = \arcsin Q, \tag{2}$$

where $Q = \text{const.} \times (v \sin i) P R^{-1}$. The error Δi of the inclination angle then becomes

$$\Delta i = \frac{\partial i}{\partial Q}\Delta Q = \left(1 - Q^2\right)^{-1/2} \Delta Q. \tag{3}$$

For low values of i, the error of i is approximately proportional to the error of Q, but for $Q \to 1$ (i.e. $i \to \pi/2$), the error becomes very large.

Inclination estimates from $v \sin i$ are also prone to systematic errors if additional line broadening effects are not properly taken into account. If additional broadening effects are overlooked, the evaluation of the line profiles tends to result in inclination angles that are systematically too large.

Of the observational input parameters of Eq. (2), the values $v \sin i$ and P can be measured fairly precisely. However, the derivation of the stellar radius R depends on parameters, such as the luminosity, the effective temperature, the reddening, and the veiling of the stars, which are often not very well known for CTTSs. Therefore, stellar radii of CTTSs derived by different authors typically differ by factors of two (see, e.g., Johns-Krull & Gafford 2002). Even with R being uncertain by that amount, for small i a useful approximation of the inclination can still be estimated from stellar rotation data. But for inclinations $i > 30$ degrees, the errors of i derived from the rotation can approach $\pi/4$. In this case the inclination essentially becomes undetermined.

In addition to observed inclinations, we present in Table 1 velocity data derived from the profiles of selected emission lines. For the forbidden lines, we provide individual references in the

---

[1] See http://circumstellardisks.org
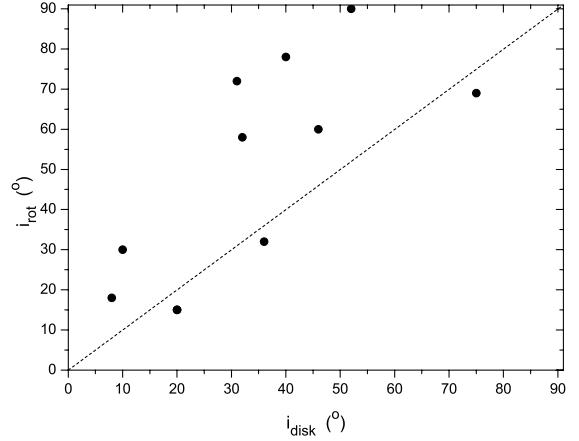
Fig. 1. Inclination angles i_{rot} derived from the stellar rotation as a function of the circumstellar disk inclinations i_{disk} of the corresponding objects.

column following the [N II] data. The mean errors of the forbidden line velocity data range between 2 km s^{-1} and about 10 km s^{-1}, with an average of about 6 km s^{-1}. The information on the profiles of the Hα and He I 587.6 nm lines was in most cases taken from Alencar & Basri (2000). For the objects not observed by these authors, the following sources were used: Beristain et al. (2001) for FP Tau, CY Tau, DD Tau, GI Tau, and HN Tau; Appenzeller et al. (2005) for HK Tau B, HH30*, and HV Tau C; Krautter et al. (1990) for VZ Cha and S CrA; Appenzeller & Wagner (1989) for GQ Lup; Alencar & Batalha (2002) for TW Hya; Hamann & Persson (1992) for HM 32; Appenzeller et al. (1986) for VV CrA; Hirth et al. (1997) for Hα of DD Tau, DH Tau, and HN Tau; Boesgaard (1984) for Hα of RU Lup; Hamilton et al. (2003) for Hα of KH15D; Stempels & Piskunov (2002) for He I 587.6 nm of RU Lup. The edge velocities of the He I 1083 nm absorption feature in the last column of Table 1 are based on the profiles published by Edwards et al. (2006). When spectra were not available in digital form, the corresponding features were measured in the published printed figures. The resulting accuracy (m.e. ≈ 10 km s^{-1}) is adequate for the statistical purposes of this study. For the blueshifted [N II] emission peak and the wind absorption feature of the Hα line, we present central velocities. For [O I] 630 nm (where the blueshifted peak is often not well defined) and for the He I 1083 nm absorption feature, we give edge velocities, as defined in the notes to Table 1. This has to be taken into account when the velocities are compared.

3. Comparison of rotational and disk inclinations

The spectral data given in Table 1 were used to search for possible correlations between the inclination and spectral properties. Initially this search was carried out separately for the inclinations based on the stellar rotation and for the inclinations of the circumstellar disks. However, for the inclination angles derived from the rotational data, no significant correlations could be detected for any of the tested spectral features. On the other hand, correlations were found, when the same spectral features were compared with the disk inclinations.

Therefore, in a next step, we used the 11 objects in Table 1 for which inclinations derived from $v \sin i$ and disk inclinations are both available to compare the inclinations derived by the two methods. As illustrated by Fig. 1, the inclinations derived by the two methods are correlated for this sample, but are clearly not identical. The mean difference between the inclinations derived

by the two methods is about 19°. More critical is that the inclinations derived from $v \sin i$ are systematically larger (by about the same amount). In three cases with $i > 30°$, the difference is about 40°, i.e., close to $\pi/4$. The average differences between the inclination angles derived by the two methods greatly exceed the observational errors given for the disk inclinations, but (in view of the errors discussed in Sect. 2) such deviations are expected for the rotation-based inclinations. Together with the fact that no correlations between the rotation-based inclinations and the spectral properties could be detected, we regard the poor agreement between the angles indicated in Fig. 1 as evidence that the rotation-based inclinations are, at present, not accurate and reliable enough for statistical studies. Therefore, the following sections will be based essentially on the disk-inclination values.

4. Correlations between the disk inclinations and spectral properties

Among the spectral features for which a correlation with inclination has been predicted most frequently are the emission lines and absorption features that are formed in the winds of the CTTSs. This applies in particular to the broad or high-velocity component of the forbidden-line profiles (see, e.g., Hartigan et al. 1995) and to the blueshifted absorption components of the hydrogen and helium permitted lines (e.g., Kurosawa et al. 2006; Beristain et al. 2001). In the following, we investigate in turn the forbidden and permitted line profiles.

4.1. Forbidden lines

The forbidden lines in CTTS spectra often have complex profiles, which vary greatly between individual objects and between different lines. However, in many cases the profiles can be deconvolved into a narrow or low-velocity component (LVC) with a typical FWHM of about 50 km s^{-1} (see Hirth et al. 1997), and a broader and usually blueshifted high-velocity component (HVC).

The HVCs are generally assumed to originate in fast outflows, which continue into the interstellar space as jets. Among the lines where the broad forbidden-line component is usually most conspicuous are the [N II] lines at 654.8 nm and 658.3 nm. In many cases, the [N II] line profiles have a well defined blueshifted peak. The absolute values of the peak velocities are usually regarded as a mean for the projected wind velocities of the [N II] emitting volumes. If available, the measured velocities of the blue [N II] 658.3 nm peaks are listed in Table 1.

At high inclinations, the blueshifted peak tends to merge with the low-velocity peak, and for edge-on objects the blueshifted peak can often not be separated from the narrow, low-velocity component. Among the objects in Table 1, this applies to HK Tau B and HH 30*. In these cases we include in Table 1 the highest value of the HVC-peak blueshift that appears to be compatible with the blue wing of the total [N II] profile. Since the corresponding velocity limits are close to zero (but – by definition – cannot be >0), they are, within the accuracy of this study, adequate approximations of the blueshifted peak velocities.

Resolved jet flows of CTTSs often form narrow and almost linear cones. Assuming that the unresolved inner [N II] flows have the same geometry, we may expect that the observed wind velocities are proportional to $\cos i$. Therefore, in Fig. 2 we plot the projected wind velocities, as inferred from the velocities of the blue [N II] peaks, as a function of $\cos(i_{\mathrm{disk}})$. The figure
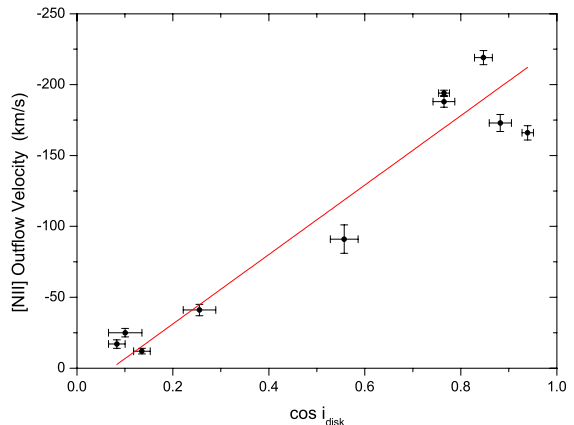
Fig. 2. Projected wind velocities inferred from the blueshifted peaks of the [N II] 658.3 nm lines as a function of the cosine of the disk inclination. Also included is the corresponding linear regression line.
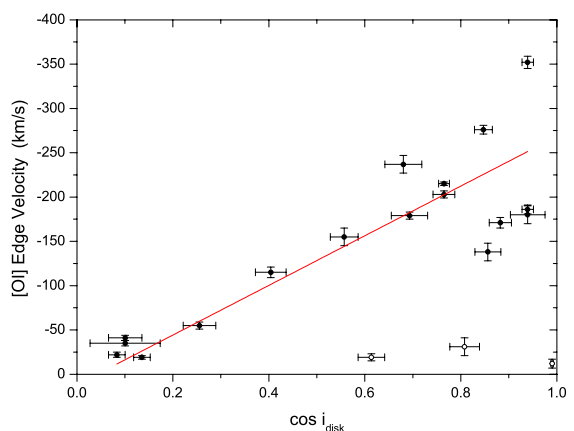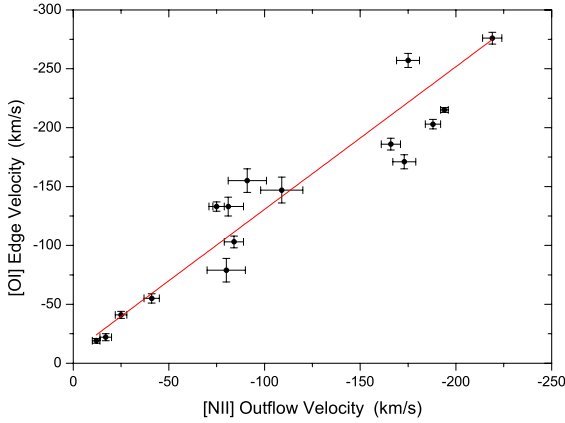

Fig. 3. Projected wind velocities inferred from the blue edges of the [O I] 630 nm lines as a function of the cosine of the disk inclination and the corresponding linear regression line. The open symbols refer to the three "weak-wind" objects BP Tau, GM Aur, and TW Hya.

shows that the observed [N II] wind velocities are clearly correlated with the disk inclinations. The correlation's adjusted coefficient of determination (which takes the error bars into account) is $\bar{R} = 0.95$. Moreover, the plot supports the assumption that the $\cos i$ -law provides a good approximation. Most of the variation in the observed velocity can obviously be explained by the varying inclination.

The projection effect is also expected to influence the apparent velocity observed in the [O I] 630 nm line, which forms under similar conditions to the [N II] line. The [O I] line tends to be stronger and is present in the spectra of practically all stars listed in Table 1. However, compared to [N II], the oxygen line has the disadvantage of often lacking a distinct blue peak, although a broad line component is usually present in the form of an extended blue wing. As a measure of the projected (maximal) wind velocity, for this line we therefore used the blue edge of the total line profile, measured at 25% intensity. In Fig. 3 this quantity is plotted as a function of $\cos(i_{\mathrm{disk}})$. Again a clear correlation is observed. However, three objects, BP Tau, GM Aur, and TW Hya fall well below the relation defined by all other stars. Therefore, these three stars are discussed separately in Sect. 4.2. If we disregard the three objects listed above, the correlation in Fig. 3 is again highly significant, with $\bar{R} = 0.91$.

Since both the blue-peak velocity of the [N II] profile and the [O I] blue-edge velocity have been found to depend on the
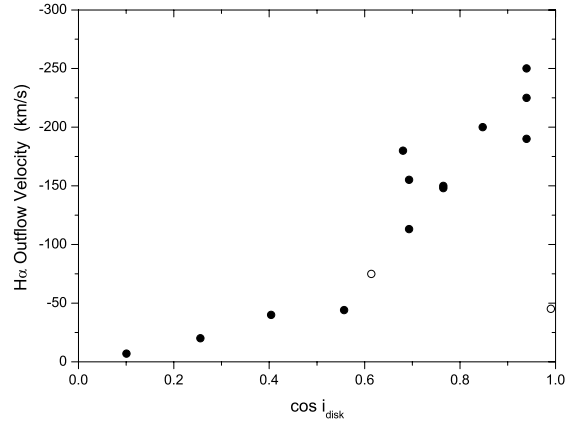
Fig. 4. Blue-edge velocities of the of the [O I] 630 nm lines as a function of the projected wind velocities indicated by the blue peak of the [N II] 658.3 nm line, and the corresponding linear regression line.

Fig. 5. Projected wind velocities inferred from the blueshifted absorption component of the Hα line as a function of the cosine of the disk inclination. Because of the time variability of the Hα profiles, errors cannot be reliably estimated for the values given for this feature. Therefore, error bars are omitted in this plot. The open symbol refers to GM Aur. Note the weak dependence on $\cos i$ of the outflow velocity for $\cos i < 0.7$.

inclination, there has to be some mutual correlation between these two quantities. This is illustrated in Fig. 4. Since the [O I] edge measures the maximal outflow velocity, it is expected to be systematically higher than the [N II] peak velocity. This is confirmed by Fig. 4, where the [O I] edge velocities are on average 25% higher than the [N II] peak velocities. The individual points in Fig. 4 deviate from the mean relation on average by only about 20 km s^{-1}. This value is not much more than the differences expected from the measuring errors alone ($\bar{R} = 0.96$ for this correlation).

4.2. Weak-wind stars

As noted above and shown in Fig. 3, the three stars BP Tau, GM Aur, and TW Hya were found to have [O I] absolute edge velocities ≤31 km s^{-1} in spite of $\cos i$ values >0.6. In all three cases, the observed [O I] edge velocity differs from the mean relation by more than 20σ. All three stars have only very weak forbidden lines without detectable broad components. In contrast to the edge-on CTTSs with narrow [O I] lines, these three stars have no detectable jets (e.g., Azevedo et al. 2007). Moreover, except for the blueshifted absorption component of the He I 1083 nm line of TW Hya, wind absorption features of the permitted lines are very weak or absent in the spectra of these stars. GM Aur and TW Hya are relatively evolved pre-main-sequence stars with estimated evolutionary ages of, respectively, 7.4 Myr and ≈10 Myr (Bertout et al. 2007; Webb et al. 1999). In the spectrum of GM Aur, the emission lines sometimes almost disappear. During such periods, GM Aur has the spectral properties of a weak-line TTS (Edwards et al. 2006). BP Tau has a lower age (3.2 Myr, according to Bertout et al. 2007). But, according to Dutrey et al. (2003), this star is "a transient object in the process of clearing its disk". Kwan et al. (2007) tentatively explained the absence of wind absorption features in the spectrum of BP Tau by an inclination effect. However, as shown later in this section, other stars with similar or higher inclinations do have wind absorption components, and an inclination effect cannot explain the weak and narrow forbidden lines of BP Tau.

In view of the low observed [O I] edge velocity and the weak wind absorption features BP Tau, GM Aur, and TW Hya, which in the following are denoted as "weak-wind stars", are indicated by open symbols in the following plots, and they are not included in graphs showing deprojected wind velocities.

Some other stars in Table 1 may also belong to the weak-wind category, although a confident assignment to this class is only possible for the three objects mentioned above, for which reliable inclination data are available. The most likely additional candidate for the weak-wind group in our sample is the CTTS GQ Lup, which is one of the best studied TTSs. High-resolution spectra of this object cover more than 35 years. All show a typical CTTS spectrum with significant mass accretion. However, the star again belongs to the more evolved TTSs (e.g., Donati et al. 2012; Johns-Krull et al. 2013). No reliable disk inclination has been reported for GQ Lup. But its rotation-based inclination (27°) is low and therefore probably not dramatically wrong (see Sect. 3). In spite of its likely low inclination, GQ Lup has a very low blueshift of its [O I] emission edge, and its [O I] 630 nm emission strength ($EW \approx 80$ mÅ) is the lowest of all objects in Table 1.

4.3. Wind absorption features of permitted emission lines

Other spectral features usually ascribed to the winds of CTTSs are the blueshifted absorption components of strong permitted emission lines. Thus, their observed velocities are expected to be correlated with the inclination, too. As shown in Fig. 5, the central velocity of the blueshifted absorption component in the blue wings of the Hα lines does, as expected, increase with $\cos(i_{disk})$. However, the relation observed in Fig. 5 clearly differs from the one found for the forbidden lines, as plotted in Figs. 2 and 3. While for the forbidden lines the apparent velocity increases more or less linearly with $\cos i$, in Fig. 5 the projected velocity remains low for approximately $\cos i < 0.7$ (corresponding to $i > 45°$) and increases steeply for smaller inclinations. Since an absorption feature requires that the line-of-sight passes through the absorbing volume, as well as through the emission source, such behavior is to be expected for a wind that is restricted to a polar flow cone (see, e.g., Edwards et al. 2006). For a point-like continuum emission source, Fig. 5 can be explained by a polar flow cone with an opening angle of 45°. However, depending on the relative sizes and distance of the absorbing and continuum emitting volumes, Fig. 5 would also be consistent with a much smaller opening angle and an extended continuum emission region.
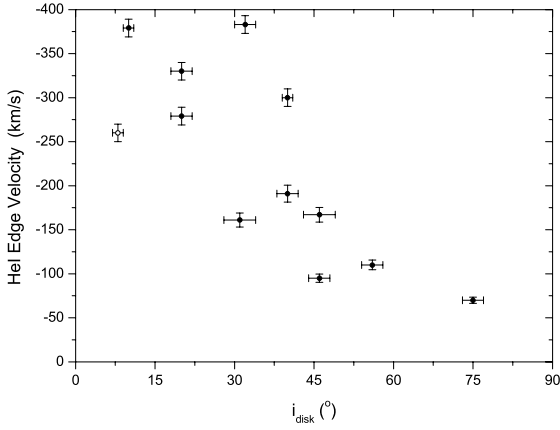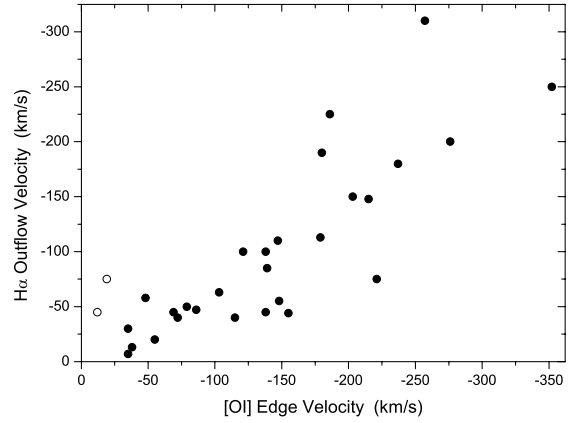
Fig. 6. Projected wind velocities inferred from the blue edge of the wind absorption component of the He I 1083 nm line as a function of the disk inclination. The open symbol refers to TW Hya.
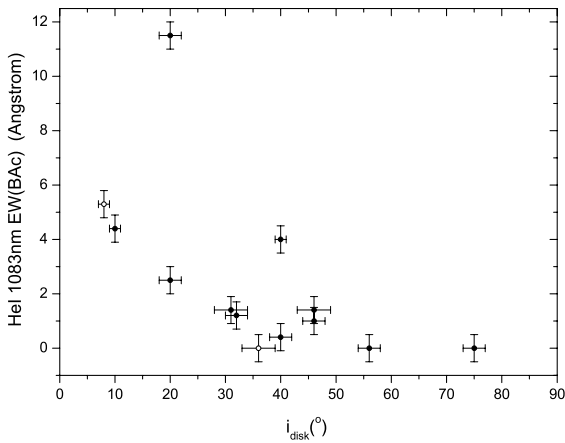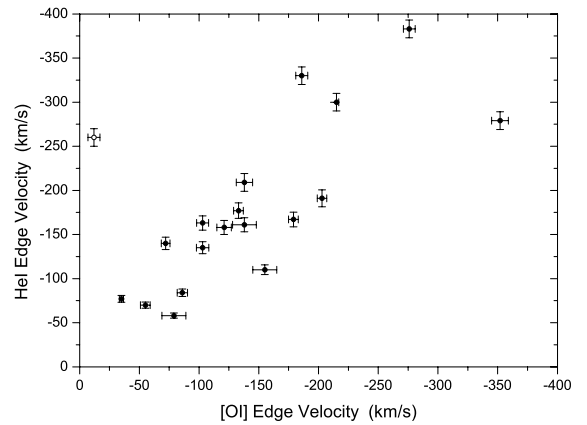

Fig. 7. Equivalent width below the continuum of the blueshifted absorption component of the He I 1083 nm line profile as a function of the disk inclination. The two open symbols refer to BP Tau and TW Hya.
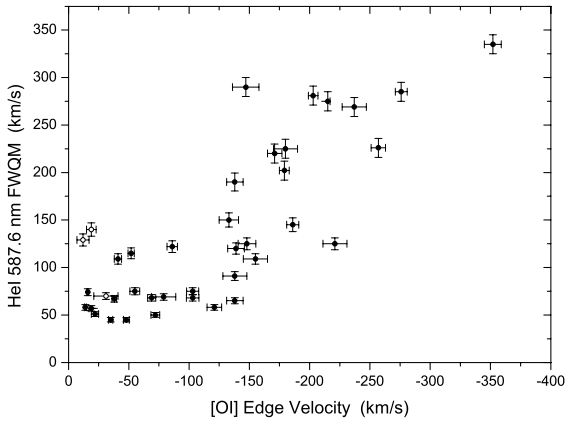

Fig. 8. Projected wind velocities inferred from the blueshifted absorption component of the Hα line as a function of the projected wind velocity indicated by the blue edge of the [O I] 630 nm line. The open symbols refer to GM Aur and TW Hya.

Fig. 9. Projected wind velocities inferred from the blue edge of the wind absorption component of the He I 1083 nm line as a function of the projected wind velocity indicated by the blue edge of the [O I] 630 nm line. The open symbol refers to TW Hya.

Among the permitted lines in TTS spectra, the He I 1038 nm line, which has a metastable lower level, is particularly well suited for studying the kinematics of absorbing gas flows. Therefore, we compare in Fig. 6 the apparent wind velocities inferred from this line with the observed disk inclinations. Since the absorption by this line usually covers a broad velocity range, and since we are mainly interested in the terminal velocity of the wind, we use the blue-edge velocity of the absorption component for this line. To have a consistent and reproducible measure, we plot the velocity where the blue wing of the wind absorption reaches 25% of the central depth in the profiles published by Edwards et al. (2006). The sample for which we have data on this spectral feature, as well as on disk inclinations, only contains one object with $\cos i < 0.5$. Therefore, we use the disk inclination angle in Fig. 6, rather than its cosine, as the abscissa. The figure again demonstrates that there is a correlation. The data points are consistent with a steep increase in the apparent wind velocity for approximately $i < 45°$ (as observed for the Hα wind absorption), but the lack of more data at high inclinations does not allow us to prove this behavior independently in the case of the He I wind absorption alone. Interestingly, the He I edge velocity of the weak-wind star TW Hya (–260 km s^{-1}, $i_{\rm disk} = 8°$) also fits the trend shown in the figure. (For the other weak-wind objects, the corresponding spectral feature is very weak or absent.)

A related correlation with the disk inclination is shown in Fig. 7, where we plot the equivalent width below the continuum of the blueshifted absorption component of the He I 1083 nm line. The corresponding data are again taken from Edwards et al. (2006). The uncertainty of the EW values has been estimated from the scatter of those cases where observations for more than one epoch have been reported. The absence of a significant absorption for inclinations >45° again supports the assumption of a cone-like outflow geometry with an opening angle ≤45°. The data point of the weak-wind star TW Hya ($EW = 5.3$ Å, $i_{\rm disk} = 8°$) again fits the trend indicated in Fig. 7.

Since the velocities of the wind absorption features and those of the forbidden lines were both found to be correlated with the inclination, we also expect correlations between the forbidden-line velocities and the wind absorption. This is confirmed in Figs. 8 and 9, where we plot our measures for the wind velocities of the permitted lines as a function of the [O I] outflow velocities. Interestingly, for the He I absorption edge, we obtain on average fairly similar projected outflow velocities to those for the [O I] emission line edge, although these features can hardly be produced in the same volumes. The central velocities of the Hα absorption features have on average only about two thirds of the [O I] edge velocities. Although at least part of the correlations indicated in Figs. 8 and 9 certainly result from

Fig. 10. Full width at one quarter of the maximum of the He I 587.6 nm emission line as a function of the projected wind velocity indicated by the blue edge of the [O I] 630 nm line. The three weak-wind objects are again indicated by open symbols.

an inclination effect, a contribution from a correlated intrinsic wind velocity cannot be excluded. But in both cases it is clear from the figures that the winds seen in both the forbidden lines and the permitted lines are physically related, in spite of the very different conditions for forming these different spectral features.

4.4. The He I 587.6 nm line width

Another permitted line that has been discussed extensively in the context of the polar winds of CTTSs is the He I 587.6 nm emission feature (see, e.g., Beristain et al. 2001; Kwan & Fischer 2011). Like the forbidden lines, this He I line often consists of both a broad and a narrow component. The broad components of the He I 587.6 nm line have widths that are comparable to those of the broad components of the forbidden lines. However, the profiles of the broad components of the helium lines are quite different from those of the broad components of the forbidden lines. While the forbidden lines often have a steep blue wing and no red wing, the broad components of the helium lines are in most cases essentially symmetric with a Gaussian-like profile. The narrow components of the helium lines are also symmetric and slightly broader than the corresponding forbidden line features. Also in contrast to the corresponding forbidden-line broad components, the broad helium-line components are only modestly blueshifted relative to the systemic velocity by about 75 km s^{-1} on average.

The broad helium emission component is often assumed to form in the T Tauri winds (e.g., Kwan & Fisher 2011). Therefore, we compared the observed widths of the He I 587.6 nm line with the disk inclinations. As a measure of the width, we used the full width of the line at a quarter of the maximal intensity (FWQM) of the total line. For the 15 objects where disk inclination data and the He I 587.6 nm line widths are listed in Table 1, we find a decrease in the line width with increasing inclination, which is to be expected when the width is related to a polar wind. However, the scatter around the mean relation is too large to regard this result as conclusive.

On the other hand, a more convincing correlation is found when the FWQM of the total He I emission is compared with the [O I] edge velocity (Fig. 10). Although the scatter of the individual data points is large, the relatively high number of data points makes the correlation significant. Since (as shown above) the [O I] velocity is well correlated with the inclination, Fig. 10

may provide indirect evidence for a relation between the maximal velocity observed in the He I 587.6 nm line[2] and the inclination, which supports a wind origin of at least part of this line emission. But the sample for which these informations are available is too limited to derive firm results. No significant correlations between the inclination and the FWHM of the broad component of the He I line (again listed in Beristain et al. 2001) and no correlation between the inclination and the intensity ratio between broad and narrow He I line components (BC/NC) could be detected, in contrast to the result for the forbidden lines. However, we suspect that such correlations do exist and could be established with larger samples.

A closer look at the individual lines reveals a qualitatively different dependence on inclination for the forbidden-line and helium-line profiles. For the forbidden lines, the broad component simply becomes narrower with increasing inclination and finally merges into the narrow component. In the case of the helium lines, broad components are found at all inclinations, although their widths and strengths decrease with increasing inclination. A good example for the different behaviors of the forbidden lines and the helium lines is the spectrum of the edge-on object HH30* ($i = 82°$), which shows a weak broad component of the He I 587.6 nm line ($FWHM \approx 140$ km s^{-1}), while a broad component of the [O I] 630 nm line is not detectable (Appenzeller et al. 2005). Similar behavior is seen in the spectrum of AA Tau ($i = 75°$).

5. Negative results

In addition to those discussed in Sect. 4, we searched for correlations between the disk inclinations and various other spectral properties, such as the strength and width of selected emission lines or line components, the veiling, and the presence and strength of redward-displaced (accretion) absorption features. Apart from some quantities that are related to the line profile data discussed in Sect. 4, no other significant correlations were detected. In contrast to a tentative result noted earlier (Appenzeller et al. 2005) and expectations from the theory (Kurosawa et al. 2006), no significant correlation could be found between the Hα equivalent width and the inclination in our larger sample with more reliable inclination angles. If such a relation exists, it is obliterated by the very large scatter in the equivalent widths of the individual stars and by the variability of this line. Larger samples will probably be needed to detect a corresponding correlation by statistical means.

A search for a correlation between the Hα FWHM line width and the inclination also ended inconclusively. Although the line widths were found to be on average lower for disk inclinations >50°, the scatter of the individual values is very large, and the result is far from being statistically significant.

We did not detect any correlation between the disk inclination and the presence or strength of the redshifted ("YY Orionis") absorption components of the He I 1083 nm line profiles observed by Edwards et al. (2006) and Fisher et al. (2008). Redshifted absorption components were found at all disk inclinations between 8° and 75°, and no dependence of their strength on the inclination is evident from the available data. The lack of such a correlation may be explained by the dependence of the accretion flows on the geometry of the magnetic fields, which in many cases is known to be tilted relative to the rotation

---

[2] Or some other measure of the broad-component width of the He I 587.6 nm line, such as the parameter V_{bwing} listed by Beristain et al. (2001).
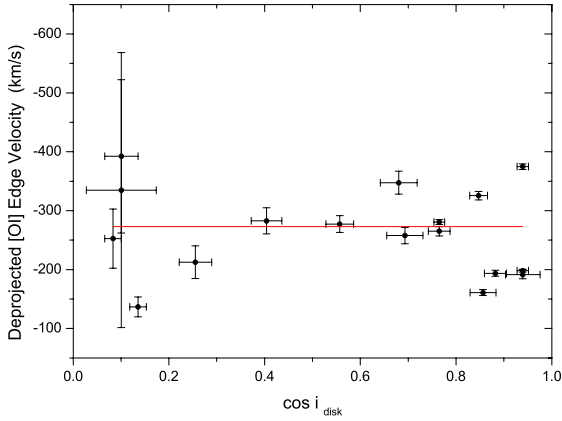
Fig. 11. Deprojected outflow velocities, as derived from the blue edge of the [O I] emission line, as a function of the cosine of the disk inclination.

axis (e.g., Bouvier et al. 2007; O'Sullivan et al. 2005). Moreover, the redshifted absorption components are known to show strong time variations, which may mask any correlation with i.
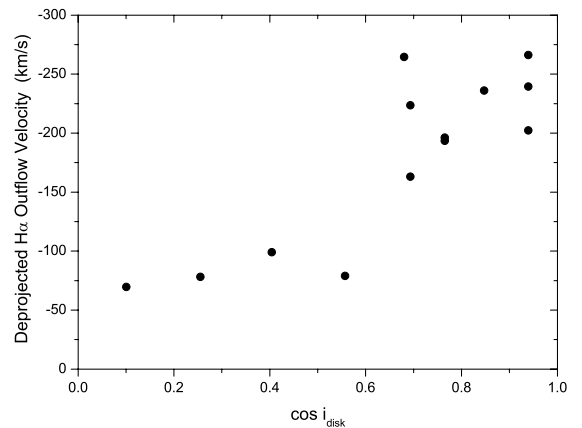
6. Deprojected wind velocities

Assuming that the polar outflows from the CTTSs are normal to the disk planes, one can derive the true, deprojected flow velocities by dividing the observed velocities by the cosine of the corresponding disk inclination, as listed in Table 1. We carried out these calculation for the [O I], [N II], Hα, and He I velocities where disk inclination data are available in Table 1. Figure 11 gives the resulting deprojected [O I] edge velocities as a function of $\cos i$. For the reasons outlined in Sect. 4, the three weak-wind TTSs have been omitted in this figure. The large error bars near the left margin of the figure result from the $(\cos i)^{-1}$ magnification of all errors for high inclinations. As shown by Fig. 11, the deprojected velocities scatter around a horizontal line. No systematic dependence of the deprojected velocities on the inclination is detected, which appears to confirm the correctness of the deprojection procedure. An error-weighted least square solution results for the complete sample of Fig. 11 in a deprojected flow velocity of 273 ± 14 km s^{-1}. A simple average of all deprojected velocities of Fig. 11 gives a flow velocity of 262 ± 18 km s^{-1}. An average of the (possibly more reliable) data for the 13 objects with $i < 80°$ ($\cos i > 0.17$) gives 258 ± 18 km s^{-1}. The median deprojected velocity of both samples is 258 km s^{-1}. All deprojected velocities range between 137 km s$^{-1} < v_{depr} < 392$ km s^{-1}. If we disregard the less certain values for $i > 80$ degrees, the range narrows to the interval 161 km s^{-1} to 374 km s^{-1}. Neglecting the results for HV Tau C and KH15D, which have errors of the deprojected velocities exceeding 100 km s^{-1}, we find that 80% of all flow velocities are in the range between 190 km s^{-1} and 350 km s^{-1}.

Deprojected velocities of the [N II] blue emission peaks are plotted in Fig. 12. Because these values correspond to to a mean flow velocity (while the [O I] data correspond approximately to the maximal flow velocity), the [N II] velocities are on average lower by about 20%. For the [N II] line, the error-weighted mean and the simple average for all objects is 196 ± 16 km s^{-1} in both cases. If only the objects with $i < 80$ degrees are averaged, we get 205 ± 14 km s^{-1}. The median value is 195.5 km s^{-1}.

In Fig. 13 we give deprojected velocities of the blue absorption component of the Hα lines. As discussed in Sect. 4, the velocities of this spectral feature behave differently for inclinations below and above about 45°. This bimodality is confirmed
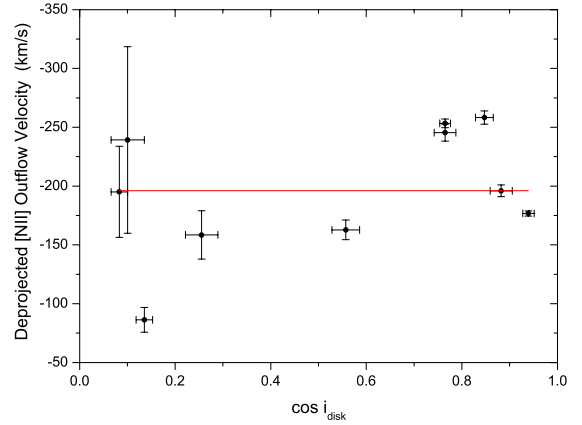
Fig. 12. Deprojected outflow velocities, as derived from the blue peak of the [N II] emission lines, as a function of the cosine of the disk inclination.


Fig. 13. Deprojected outflow velocities indicated by the blueshifted absorption components of the Hα line profiles as a function of the cosine of the disk inclination.

by Fig. 13, which indicates a low deprojected velocity for high inclinations ($\cos i < 0.68$) and high velocities for smaller inclinations. The pattern is again consistent with the assumption of a fast polar wind with a cone-like geometry and an opening angle $\leq 45°$. The mean flow velocity derived from the Hα blue absorption components with $\cos i_{disk} > 0.68$ is 224 ± 11 km s^{-1}, which is slightly higher than the average [N II] (peak) flow velocity, but lower than the mean deprojected [O I] flow velocity.

Deprojected flow velocities were also calculated for the blue-edge velocities of the He I 1083 nm absorption components. The scatter of the resulting data with $\cos i > 0.68$ is larger than in the case of the [O I] emission line edges, but the mean value 292 ± 33 km s^{-1} is (within the error limits) compatible with the [O I] result.

7. Correlations with other stellar parameters

The scatter of the deprojected flow velocities of the forbidden lines is clearly greater than can be explained by the observational errors alone. Thus, assuming that the disk inclination errors cited in the literature are correct, we have to conclude that significant, real differences exist between the outflow velocities of the individual objects. To clarify the origin of these differences, we searched for correlations between the individual deprojected velocities and other stellar properties. In detail, we checked for possible correlations between these velocities and
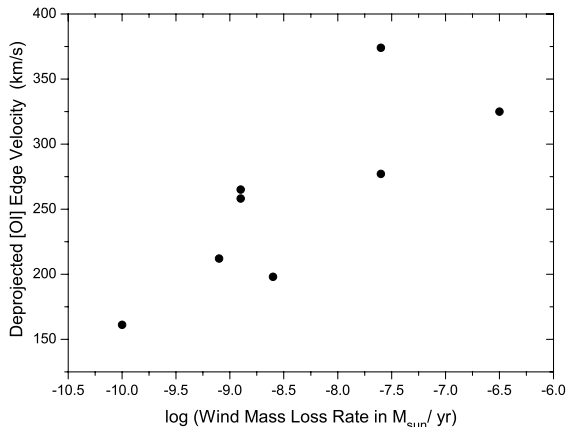
Fig. 14. Deprojected wind flow velocities inferred from the blue edge of the [OI] 630 nm lines as a function of the logarithm of the wind mass loss rate.

the objects' escape velocities, photospheric radii, rotation periods, magnetic field data, spectral veiling, mass accretion rates, wind mass loss rates, and various line profile properties. No convincing correlations could be found. A trend, shown in Fig. 14, was found for the relation between the deprojected [O I] velocity and the wind mass loss rate as listed by Hartigan et al. (1995). The flow velocity appears to increase systematically from about 200 km s^{-1} at $\dot{M} = -10^{-10}$ $M_\odot$/yr to ≈400 km s^{-1} at about $\dot{M} = -3 \times 10^{-7}$ $M_\odot$/yr. However, this result is only based on eight data points. Perhaps more remarkable may be that the velocity change is only a factor two, while the mass loss rate changes by about 3×10^3.

That no other correlations of the deprojected velocity with stellar parameters could be detected does not rule out that such correlations exist. In most cases the detection of significant correlations was precluded by the smallness of our samples and/or by too large errors of the input data. Additional data will be needed to find correlations with other stellar parameters and to clarify the origin of the differences in outflow velocities.

8. Conclusions

The results described in the previous sections show that various properties of the spectra of CTTSs are correlated with the inclinations of their associated circumstellar disks. No such correlations could be detected for inclinations derived from the rotational data of these stars, and the correlation between the rotation-based inclinations and the disk inclinations is rather poor. This seems to indicate that only the disk inclinations provide a good measure of the true orientations of the TTS systems, while the values derived from stellar rotation data are not yet accurate enough for such studies.

The most conspicuous correlations with the disk inclination are observed for the profiles of the forbidden emission lines and for the velocities of the wind absorption features of some permitted lines. The data support the assumption of cone-like fast polar winds with opening angles ≤45°. A correlation is also indicated between the disk inclination and the width of the He I 587.6 nm emission line. This supports earlier suggestions that this line is at least in part related to the T Tauri winds.

Using the disk inclination values, true (deprojected) wind flow velocities were calculated. From the blue edge of the [O I] emission, we find mean flow velocities of about 260 km s^{-1}, with the well determined individual values ranging between

161 km s^{-1} and 374 km s^{-1}. The blue edges of the wind absorption features of the He I 1083 nm line give similar mean values, although the scatter of the individual velocities is greater. The deprojected central velocities of the Hα wind absorption components have velocities that are similar to or slightly larger than those derived from the blueshifted emission peaks of the [N II] lines. The derived deprojected flow velocities differ among the observed objects. Correlations of these differences with other stellar parameters could not be reliably established with the samples that are presently available. Larger samples, which will probably become available with future ALMA observations of TTS disks, may provide answers to this question.

References

Akeson, R. L., Millan-Gabet, R., Ciardi, D. R., et al. 2011, ApJ, 728, 96
Alencar, S. H. P., & Basri, G. 2000, AJ, 119, 1881
Alencar, S. H. P., & Batalha, C. 2002, ApJ, 571, 378
Alencar, S. H. P., Johns-Krull, C. M., & Basri, G. 2001, AJ, 122, 3335
Andrews, S. M., & Williams, J. P. 2007, ApJ, 659, 705
Appenzeller, I., & Wagner, S. 1989, A&A, 225, 432
Appenzeller, I., Jankovics, I., & Jetter, R. 1986, A&AS, 64, 65
Appenzeller, I., Bertout, C., & Stahl, O. 2005, A&A, 434, 1005
Azevedo, R., Folha, D. F. M., Gameiro, J. F., et al. 2007, ApJ, 670, 1234
Beristain, G., Edwards, S., & Kwan, J. 2001, ApJ, 551, 1037
Bertout, C., Basri, G., & Bouvier, J. 1988, ApJ, 330, 350
Bertout, C., Siess, L., & Cabrit, S. 2007, A&A, 473, L21
Boesgaard, A. M. 1984, AJ, 89, 1635
Böhm, K.-H., & Solf, J. 1994, ApJ, 430, 277
Bouvier, J., Covino, E., Kovo, O., et al. 1995, A&A, 299, 89
Bouvier, J., Alencar, S. H. P., Boutelier, T., et al. 2007, A&A, 463, 1017
Broeg, C., Schmidt, T. O. B., Guenther, E., et al. 2007, A&A, 468, 1039
Camenzind, M. 1990, Rev. Mod. Astron., 3, 234
Cox, A. W., Grady, C. A., Hammel, H. B., et al. 2013, ApJ, 762, 40
Curiel, S., Raga, A., Raymond, J., et al. 1997, AJ, 114, 2736
Donati, J.-F., Gregory, S. G., Alencar, S. H. P., et al. 2012, MNRAS, 425, 2948
Dutrey, A., Guilloteau, S., & Simon, M. 2003, A&A, 402, 1003
Edwards, S., Hartigan, P., Ghandour, L., & Andrulis, C. 1994, AJ, 108, 1056
Edwards, S., Fischer, W., Hillenbrand, L., & Kwan, J. 2006, ApJ, 646, 319
Fischer, W., Kwan, J., Edwards, S., & Hillenbrand, L. 2008, ApJ, 687, 1117
Guilloteau, S., Dutrey, A., Piétu, V., & Boehler, Y. 2011, A&A, 529, A105
Hamann, F. 1994, ApJS, 93, 485
Hamann, F., & Persson, S. E. 1992, ApJS, 82, 247
Hamilton, C. M., Herbst, W., Mundt, R., et al. 2003, ApJ, 591, L45
Hartigan, P., Edwards, S., & Ghandour, L. 1995, ApJ, 452, 736
Hartmann, L., Hewett, R., & Calvet, N. 1994, ApJ, 426, 669
Herczeg, G. J., Najita, J. R., Hillenbrand, L. A., & Pascucci, I. 2007, ApJ, 670, 509
Hirth, G. H., Mundt, R., & Solf, J. 1997, A&AS, 126, 437
Isella, A., Carpenter, J. M., & Sargent, A. I. 2010, ApJ, 714, 1746
Johns-Krull, C. M., & Gafford, A. D. 2002, ApJ, 573, 685
Johns-Krull, C. M., Chen, W., Valenti, J. A., et al. 2013, ApJ, 765, 11
Krautter, J., Appenzeller, I., & Jankovics, I. 1990, A&A, 236, 416
Kurosawa, R., Harries, T. J., & Symington, N. H. 2006, MNRAS, 370, 580
Kurosawa, R., Romanova, M. M., & Harries, T. J. 2011, MNRAS, 416, 2623
Kwan, J., & Fischer, W. 2011, MNRAS, 411, 2383
Kwan, J., Edwards, S., & Fischer, W. 2007, ApJ, 657, 897
Kwon, W., Looney, L. W., & Mundy, L. G. 2011, ApJ, 741, 3
Muzerolle, J., Calvet, N., & Hartmann, L. 2001, ApJ, 550, 944
O'Sullivan, M., Truss, M., Walker, Ch., et al. 2005, MNRAS, 358, 632
Ratzka, T., Chen, W., Valenti, J. A., et al. 2009, A&A, 502, 623
Roccatagliata, V., Ratzka, T., Henning, T., et al. 2011, A&A, 534, A33
Schegerer, A. A., Wolf, S., & Hummel, C. A. 2009, A&A, 502, 367
Shevchenko, V. S., Grankin, K. N., Mel'Nikov, S. Yu., et al. 1998, Astr. Lett., 24, 528
Stapelfeldt, K. R., Krist, J. E., Menard, F., et al. 1998, ApJ, 502, L65
Stapelfeldt, K. R., Ménard, F., Watson, A. M., et al. 2003, ApJ, 589, 410
Stempels, H. C., & Piskunov, N. 2002, A&A, 391, 595
Tanii, R., Itoh, Y., Kudo, T., et al. 2012, PASJ, 64, 124
Weaver, W. B. 1987, ApJ, 319, L89
Webb, R. A., Zuckerman, B., Platais, I., et al. 1999, ApJ, 512, L63
Yorke, H. W., Bodenheimer, B., & Laughlin, G. 1993, ApJ, 411, 274